

Body torque modulation for a microrobotic fly

Benjamin M. Finio, *Student Member, IEEE*, Jessica K. Shang and Robert J. Wood, *Member, IEEE*

Abstract—The Harvard Microrobotics Lab has previously demonstrated the world’s first at-scale robotic insect capable of vertical takeoff with external power. Both of the robot’s wings were driven by a single power actuator and 1-DOF mechanical transmission – making independent control of both wings, and therefore asymmetric flapping and the generation of a net body torque, impossible. This paper presents a method to modulate body torques by altering the kinematics of each wing transmission independently, via the introduction of two additional control actuators. Theoretical kinematic and dynamic predictions based on a pseudo-rigid body model are compared to the observed wing trajectories. Controllable body torques are necessary for the development of control algorithms for eventual stable hovering and free flight.

I. INTRODUCTION

Autonomous micro air vehicles (MAVs) are of great interest for applications such as reconnaissance, hazardous environment exploration, and search and rescue missions. The unsteady forces associated with flapping-wing flight may offer increased maneuverability at small scales compared to fixed or rotary wing designs. The Harvard Microrobotics Lab has taken a first step towards the development of such autonomous MAVs through the creation of the world’s first insect-sized MAV capable of vertical liftoff with external power and control [1], [2], [3]. The fly consists of four main components, each with an analog in the thoracic mechanics of flying insects: the airframe (exoskeleton), actuator (flight muscle), transmission (thorax), and wings. These components are manufactured using the Smart Composite Microstructures paradigm which uses high stiffness-to-weight ratio materials (e.g. carbon fiber), and thin polymer films to create flexure hinges which act as low-loss revolute joints. The use of discretized compliances allows analysis of the kinematics and dynamics using pseudo-rigid body methods [4]. The complete fly is shown in Fig. 1.

The first generation of the Harvard microrobotic fly uses a single piezoelectric bimorph cantilever beam as a power actuator [5], [6] to drive a 1-DOF mechanical transmission that flaps both wings symmetrically. A flexure hinge and passive dynamics allow each wing to also rotate about an axis parallel to the spanwise direction, creating an underactuated 3-DOF system. Other, larger-scale MAVs use a single DC motor and 1-DOF crank-rocker transmission to flap both wings [7], [8], while using rudders and elevators to steer via thrust vectoring [9]. This is in contrast to prior attempts at insect-sized MAVs such as the Berkeley Micromechanical Flying Insect (MFI), which used four actuators (one for

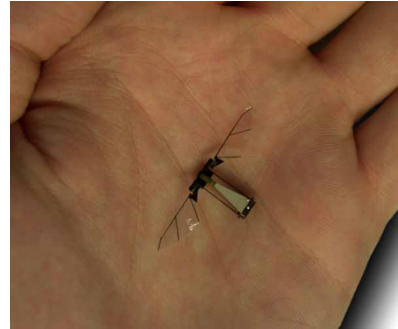


Fig. 1. The Harvard Microrobotic Fly, a 60 mg, 3-cm wingspan MAV capable of vertical liftoff with external control and power.

each DOF) to control the 2-DOF trajectory of each wing independently [10], [11], [12]. This resonant two-input two-output system presents a much greater design and fabrication challenge to match the resonant frequencies of the two rotational motions (flapping and rotation about the spanwise axis). Driving one rotational motion off-resonance will result in wasted energy fighting the coupled system dynamics.

While the underactuated system presents a challenge from a control standpoint, it greatly simplifies the design and fabrication process. It also takes advantage of passive system dynamics to allow the pronation and supination of the wing at the ends of each stroke. There is evidence to suggest that wing rotation in insects, while partially driven by active flight muscles, is enhanced by aerodynamic and inertial forces [13]. The aerodynamic effects resulting from the wing rotation contribute to the superior maneuverability of flying insects [14], which currently surpasses anything manmade – thus the motivation to first mimic, then improve upon the dynamics of insect flight in robotic designs.

While much work has been done to develop and simulate control algorithms for the Berkeley MFI [15], [16], [17], [18], preliminary work on the Harvard microrobotic fly focused on achieving liftoff by minimizing weight and maximizing the propulsive efficiency. Since both wings are driven by the same power actuator and a symmetric 1-DOF mechanical transmission, flapping is ideally symmetric (though manufacturing imperfections exist) and thus generation of net body torques is impossible. As a step toward developing control laws for stable hovering, it is desirable to develop a method to independently modulate the trajectory, and thus the resulting forces, of each wing while continuing to utilize passive rotation and thus avoiding the need for additional power actuators. One possible solution is the introduction of two “control” actuators, to change the 1-DOF transmission to 3-DOF (Fig. 2), creating a 5-DOF system (one power, two

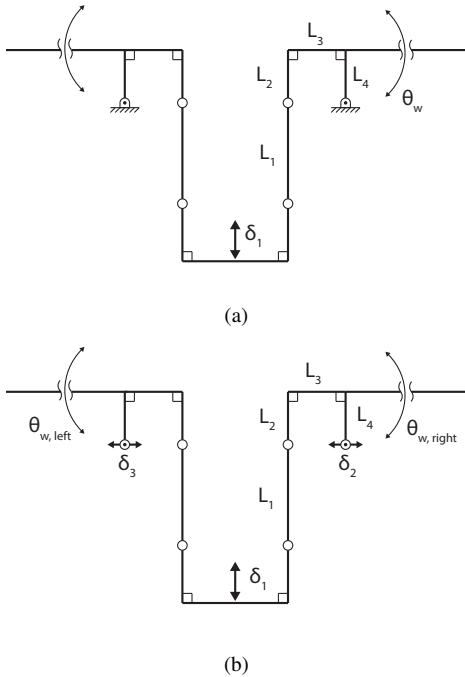


Fig. 2. In the original microrobotic fly design, both wings are driven by a single power actuator δ_1 through a 1-DOF symmetric transmission, resulting in symmetric flapping θ_w (a). The pivots at the base of each wing are connected to ground, i.e. the airframe. In the proposed design, the wing pivots are connected to two new control actuators (which are then connected to ground) - creating control inputs δ_2 and δ_3 (b). This allows independent modulation of each side of the transmission.

control, two passive). A single power actuator will still act as the primary source of mechanical power for flapping, while two control actuators modify transmission kinematics independently, creating asymmetries in wing motion. The small displacement of the wing pivot required to alter the wing kinematics means the control actuators can be significantly lower power and mass than the power actuator. This actuation method, dubbed “orthogonal actuation spaces”, is directly analogous to Dipteran thoracic mechanics, in which large indirect power muscles are the primary source of mechanical energy, and small adjustments to the thorax are made using direct control muscles for steering purposes [19].

II. KINEMATICS

Since the transmission is symmetric, it is sufficient to derive the forward kinematics for only one side, mapping the linear input from the power actuator to the flapping motion of the wing. This was first done by Wood in [2] and is expanded here to include the second input from the control actuator. Thus, the stroke angle of the wing, θ_w , can be given explicitly as a function of the two linear actuator inputs, δ_1 and δ_2 (power and control, respectively - note the sign conventions that positive θ_w corresponds to positive δ_1 , and δ_2 is positive outward away from the vehicle center of mass). Note that in [2], L_2 and L_4 are assumed to be equal, so the expression

presented here is somewhat more complicated:

$$\begin{aligned} \theta_w = & -\frac{\pi}{2} + \arccos \left[\left((L_3 + \delta_2)^2 + (L_1 + L_2 - L_4 - \delta_1)^2 \right. \right. \\ & \left. \left. + L_3^2 + (L_2 - L_4)^2 - L_1^2 \right) \left(2\sqrt{L_3^2 + (L_2 - L_4)^2} \times \right. \right. \\ & \left. \left. \sqrt{(L_3 + \delta_2)^2 + (L_1 + L_2 - L_4 - \delta_1)^2} \right)^{-1} \right] \\ & + \arctan \left(\frac{L_3 + \delta_2}{L_1 + L_2 - L_4 - \delta_1} \right) \\ & + \arctan \left(\frac{L_2 - L_4}{L_3} \right) \end{aligned} \quad (1)$$

where L_i are the respective link lengths as shown in Fig. 2.

Previously, the primary design consideration was maximizing the total stroke angle in order to maximize lift. This was done by defining a transmission ratio, T , as the ratio of angular motion of the wing per unit input of power actuator displacement; and maximizing that ratio based on the forward kinematics. A secondary goal is *symmetric* flapping, meaning that the mean stroke angle is approximately zero. This ensures that the center of lift vector (averaged over one wing stroke) for the two wings intersects with the body’s center of mass, preventing undesired generation of a net pitch torque (Fig. 3a). With a single actuator, the total and mean stroke angles could be adjusted for both wings symmetrically by changing the amplitude and DC offset, respectively, of the driving voltage signal (see [6] for details). This allowed modulation of the thrust vector and torque about the pitch axis only (Fig. 3b).

The introduction of a second degree of freedom to each side of the transmission allows coupled modulation of both stroke amplitude and mean stroke angle. The lift force on a wing will increase with wing velocity, so it follows that increasing stroke amplitude while holding frequency constant will increase lift. This means that asymmetrically changing the wing stroke amplitudes will create asymmetric lift forces, and thus a net body torque about the yaw axis (Fig. 3b). It will be shown later that control actuator motion has a much larger effect on total stroke angle than mean stroke angle, thus can effectively be used to control torques about the yaw axis independent of the pitch torque. In conjunction with changing the DC offset of the power actuator signal to control torques about the pitch axis, this gives controllability of torques about two of the three body axes. The generation of roll torques requires some degree of control over delayed or advanced rotation of the wing at the end of each stroke (or completely independent control of the wings with two power actuators), and is beyond the scope of this paper.

As a design parameter for the new transmission, it is useful to define another quantity in addition to the transmission ratio - the control power C . This is defined as the *change* in total stroke angle per unit displacement of the control actuator:

$$C = \frac{\Delta\theta_{total}}{\delta_2} \quad (2)$$

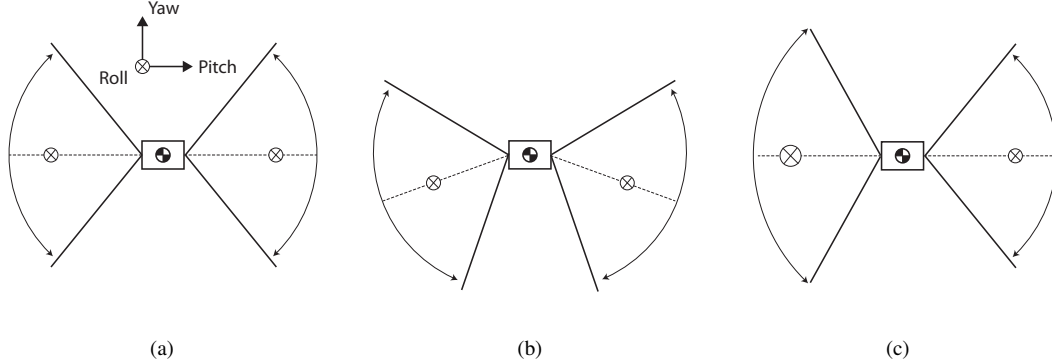


Fig. 3. In the first generation design (a), the center of lift could be shifted forward or backward relative to the body’s center of mass to create pitch torques (b). With the addition of control actuators, lift forces on each wing can be modulated asymmetrically to generate yaw torques (c).

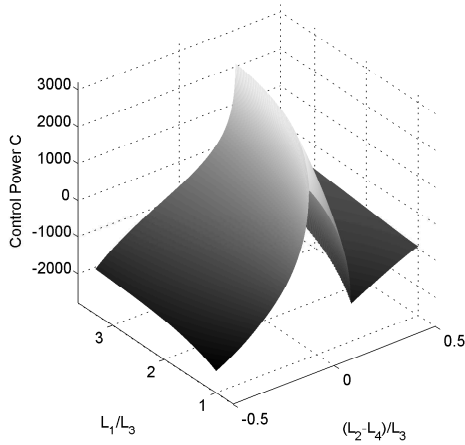


Fig. 4. Control power C is plotted as a function of nondimensional transmission geometric parameters L_1/L_3 and $(L_2 - L_4)/L_3$, with fixed actuator inputs $\pm\delta_1$ and $\pm\delta_2$.

In addition to maximizing the transmission ratio to achieve higher lift, it is also desirable to maximize the control power. It is shown in [2] that T depends primarily on L_3^{-1} ; thus, as a starting point for the new design, L_3 is minimized in order to maximize T (the lower bound being $300\mu\text{m}$ due to manufacturing limitations). It can be seen in (1) that (a) the kinematics are scale-invariant and (b) only the relative value $L_2 - L_4$, not the absolute value of L_2 or L_4 , is significant. Therefore C can be calculated as a function of two nondimensional variables, L_1/L_3 and $(L_2 - L_4)/L_3$, assuming a fixed power actuator input $\pm\delta_1$ and control actuator range $\pm\delta_2$. The objective is then to find the maximum absolute value of C and choose the corresponding transmission geometry (Fig. 4). The peak in the plot indicates that the transmission will pass through a singularity, which is undesirable. Therefore, designs near the peak are avoided, despite the relatively large value of C . The following geometry is selected to give $|C| \approx 2000 \text{ rad}\cdot\text{m}^{-1}$: $L_1 = 400\mu\text{m}$, $L_2 = 300\mu\text{m}$, $L_3 = 300\mu\text{m}$, and $L_4 = 450\mu\text{m}$.

Once the transmission design is selected, (1) can be used to calculate the expected wing trajectory over fixed ranges for

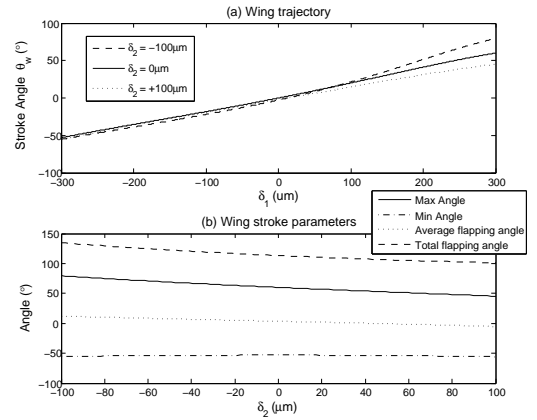


Fig. 5. Wing angle as a function of power actuator displacement δ_1 for various fixed δ_2 (a); maximum, minimum, mean and total stroke angles for a range of δ_2 and fixed $\delta_1 = \pm 300\mu\text{m}$ (b).

the power and control actuators (Fig. 5). The kinematics predict that, holding power actuator input constant at $\pm 300\mu\text{m}$, a change in total stroke angle of $\sim 30^\circ$ can be achieved with $\pm 100\mu\text{m}$ control actuator motion.

Based on the selected transmission geometry, actuators can be designed to generate the desired total stroke angle (120°). Actuator geometry can be selected based on the model shown in [6] to give the desired displacement, stiffness, and blocked force while minimizing mass and thus optimizing energy density. The actuators used here are over-designed to have a larger force and displacement than is required, allowing the device to serve as a robust testbed for the orthogonal actuation method. A future flightweight version of the fly will utilize actuators that have been designed for optimal energy density. The power and control actuators are shown in Fig. 6, and the relevant design parameters are shown in Table I.

III. DYNAMICS

While the transmission kinematics are a useful design tool, they assume the power actuator acts as a linear displacement

TABLE I
POWER AND CONTROL ACTUATOR DESIGN PARAMETERS.

	Power Actuator	Control Actuator
Mass (mg)	143	41
$\pm\delta_1$ (μm)	415	110
k (N/m)	514	2094
F_b (mN)	430	473

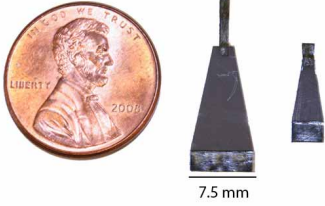


Fig. 6. The power (left) and control (right) piezoelectric bimorph actuators.

source. While the unloaded actuator tip displacement can be predicted [6], under loading conditions it is more realistic to model the actuator as a sinusoidal force input. This also allows us to analyze the effects of drive frequency and system resonance, which cannot be done with the kinematic model. This can be accomplished through the use of an Euler-Lagrange formulation:

$$\frac{d}{dt} \left(\frac{\partial L}{\partial \dot{q}} \right) - \frac{\partial L}{\partial q} = \frac{\partial W_{ext}}{\partial q} \quad (3)$$

where $L = KE - PE$, W_{ext} is the work done on the system and q is a generalized system position vector, the size of q being equal to the number of degrees of freedom of the system (for an example showing the full derivation of the Euler-Lagrange formulation for the Berkeley MFI, see [20]). Holding the control actuator position fixed as a parameter reduces the transmission system to 1-DOF; either θ_w or δ_1 can be used as the generalized position coordinate since they are related explicitly via (1). It will be seen later that it is more convenient to work in the wing space than the actuator space, meaning (3) will evaluate to a nonlinear second-order ODE in θ_w :

$$\ddot{\theta}_w = f(\theta_w, \dot{\theta}_w, t) \quad (4)$$

This necessitates writing the system kinetic energy, potential energy, and work terms as functions of θ_w and time. The actuator's applied force, stiffness due to elastic deformation, damping due to hysteresis, and work done on the system are given as:

$$F_{act} = F_b \sin(\omega \cdot t) \quad (5)$$

$$F_{spring} = -k_{act} \delta_1 \quad (6)$$

$$F_{damp} = -b_{act} \dot{\delta}_1 \quad (7)$$

$$dW_{act} = (F_{act} + F_{spring} + F_{damp}) d\delta_1 \quad (8)$$

where F_b is the actuator blocked force, ω is the frequency of the driving voltage signal, and k_{act} and b_{act} are the actuator's equivalent linear spring and damping constants, respectively. Equations (6-8) can be written in terms of θ_w

via the inverse of (1) for consistency with the selection of q in the Euler-Lagrange formulation. Using the full nonlinear kinematic equation becomes computationally expensive due to the complicated nature of the derivatives, therefore a quadratic fit is used:

$$\delta_1 = A\theta_w^2 + B\theta_w + C \quad (9)$$

where A, B and C are intrinsic functions of δ_2 . The kinetic energies of the transmission and actuator are negligible compared with that of the wings, and the stiffness of the flexure hinges is negligible relative to the actuator, and thus these terms are ignored. The kinetic energy of the wing is given as:

$$KE_{wing} = \frac{1}{2} v \cdot (Jv) \quad (10)$$

where v is the rotational velocity vector and J is the inertia tensor about the pivot point at the base of the wing. The wing has two rotational degrees of freedom – stroke angle θ_w and angle of attack α . The angle of attack can be correlated to stroke angle by empirical observation of previous passive-rotation versions, and is shown to be about 45° at the mid-stroke ($\theta_w = 0$) and 90° at the ends of the stroke ($|\theta_w| = \theta_{w,max}$), giving the following form:

$$\alpha = \frac{\pi}{2} - \frac{\pi}{4} \cos \left(\arcsin \left(\frac{\theta_w}{\theta_{w,max}} \right) \right) \quad (11)$$

A quasi-steady blade element method [21] can then be used to approximate the aerodynamic force on the wing:

$$C_N = a \cdot \sin(\alpha) \quad (12)$$

$$C_T = b \cdot \cos^2(2\alpha) \quad (13)$$

$$F_N = c \cdot \dot{\theta}_w^2 C_N \quad (14)$$

$$F_T = c \cdot \dot{\theta}_w^2 C_T \quad (15)$$

where C_N and C_T are the force coefficients for the normal and tangential forces on the wing (F_N and F_T respectively), and a, b, and c are constants that depend on wing geometry. The drag and lift forces can then be written as follows:

$$\begin{bmatrix} F_{drag} \\ F_{lift} \end{bmatrix} = R(\alpha) \begin{bmatrix} F_n \\ F_t \end{bmatrix} \quad (16)$$

where $R(\alpha) \in SO(2)$. The lift force acts perpendicular to the plane of the transmission, therefore does no work against the actuator and is not included in the energy formulation. The drag force is exerted in the plane of the transmission and acts as a damping force against the actuator. The work done by the drag force is given by:

$$dW_{drag} = F_{drag} r_{cp} d\theta_w \quad (17)$$

where r_{cp} is the radius from the base of the wing to the aerodynamic center of pressure.

The terms in (6)-(17) can be inserted into the Euler-Lagrange formulation (3), which evaluates to the full equation shown in (18); where $\psi = \frac{\pi}{2} - \alpha$, and the $\text{sign}(\dot{\theta}_w)$ term ensures that the drag force always does negative work on the system (by convention, F_{drag} is defined to always be positive). Equation (18) can then be solved numerically

$$\ddot{\theta}_w = \left[\left(F_0 \sin(\omega t) - b_{act} \dot{\delta}_1 - k_{act} \delta_1 \right) \frac{\partial \delta_1}{\partial \theta_w} - \left(ca \theta_w^2 \sin^2(\alpha) + cb \theta_w^2 \cos^3(\alpha) \right) r_{cp} \cdot \text{sign}(\dot{\theta}_w) - \frac{\pi^2 \theta_w \dot{\theta}_w \cos(\psi) \sin(\psi)}{16 \psi \theta_{w,max}^2} (J_{zz} - J_{yy}) \right] (J_{yy} \cos^2(\psi) + J_{zz} \sin^2(\psi))^{-1} \quad (18)$$

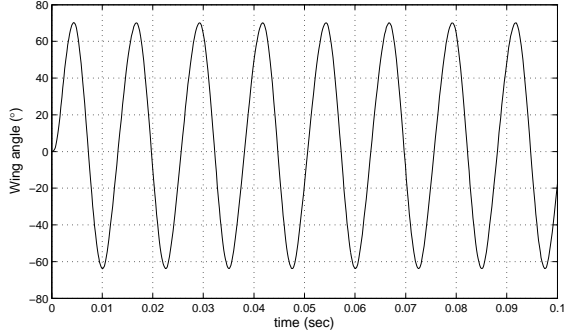


Fig. 7. Wing trajectory as a function of time, solved numerically using (18). Actuator drive frequency is 80Hz.

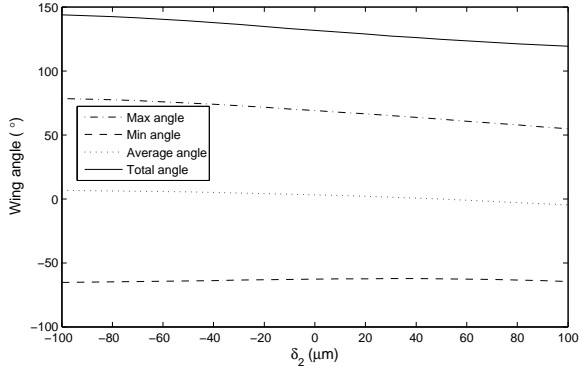


Fig. 8. Numerical simulation results showing maximum, minimum, mean and total stroke angles over the range of the control actuator motion, while holding the power actuator's driving force and frequency constant at 80Hz.

to give the wing position as a function of time (Fig. 7). As expected with a sinusoidal driving force, the output displacement is sinusoidal with an amplitude of roughly $\pm 70^\circ$.

As with the kinematics, it is of interest to determine the effects of control actuator motion on the total and mean stroke angles, which will then determine body torques. This can be done by running multiple simulations with a fixed driving force and frequency, and varying δ_2 as an input parameter (Fig. 8). The results follow the same trend as is predicted by the kinematic model (Fig. 5), showing a change in total flapping of 24° and a very small change in mean stroke angle over the full range of the control actuator.

The dynamic simulation can also be used to determine the frequency response of the system over the range of the control actuator motion (Fig. 9). This shows that the control actuator is expected to have a large impact on the system resonant frequency, shifting the resonant peak from 55Hz at $\delta_2 = -100\mu\text{m}$ to 100Hz at $\delta_2 = +100\mu\text{m}$. It also confirms

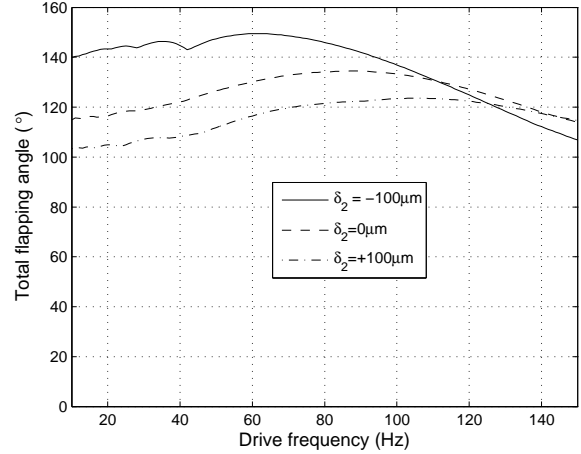


Fig. 9. Frequency response of the system over the range of control actuator motion, $\delta_2 = \pm 100\mu\text{m}$. The resonant peak is shown to shift from approximately 55 to 100Hz.

that, for frequencies $< 105\text{Hz}$, the control actuator motion will increase flapping amplitude with $\delta_2 < 0$ and decrease it with $\delta_2 > 0$, as predicted by the kinematics. For frequencies above 100 Hz, dynamic effects may dominate and the purely kinematic model may not be valid for predicting wing motion, as $\delta_2 < 0$ is shown to actually *decrease* total stroke angle. Also note that, below about 40Hz, sub-harmonic effects become prominent; however the aerodynamic forces generated at lower frequencies will be insufficient for flight, so this regime is not a concern.

Note that this dynamic model is for one side of the transmission only and assumes that the second control actuator remains fixed or is nonexistent ($\delta_3 = 0$). In practice, the addition of a second control actuator would be redundant from a control standpoint, but would allow the magnitude of yaw torques to be increased. In that case it would be necessary to examine resonant effects as a function of both δ_2 and δ_3 .

Finally, (16) can be time-averaged to estimate the average lift force on each wing. Assuming δ_2 varies for one wing while holding δ_3 constant, and that the radius to the aerodynamic center of pressure, r_{cp} is known ($\sim 10.7\text{mm}$), this can be used to predict resultant body torques about the yaw axis. The average total lift (both wings) for $\delta_2 = \delta_3 = 0$ is 1.2mN, which is in accordance with experimental measurements from [2]. The lift force on one wing can be varied from .5-.8mN with control actuator motion (Fig. 10a). This means body torques up to 1.7mN-mm can be generated with the motion of only one control actuator (Fig. 10b).

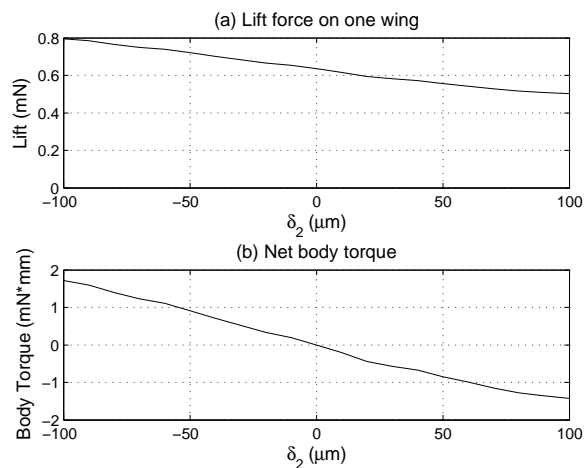


Fig. 10. Variation in lift force on one wing with control actuator motion (a) and net body torque generated about the yaw axis assuming δ_3 is held constant while δ_2 is varied (b).

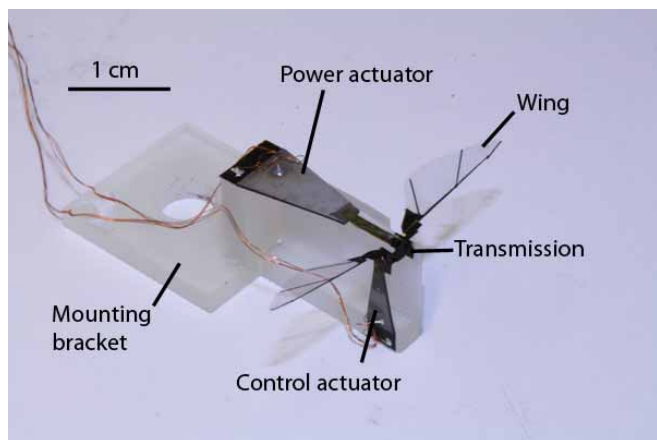


Fig. 11. The complete test setup.

IV. RESULTS AND ANALYSIS

The complete test apparatus is shown in Fig. 11. Rather than a lightweight airframe, the actuators and transmission were mounted to a rapid-prototyped acrylic block. Only one control actuator was used, with the opposite wing pivot being attached to ground.

High-speed video of the wing flapping was taken (Fig. 12) and the wing trajectories were extracted using a custom Matlab script, in order to compare to the trajectories predicted by the kinematic and dynamic analyses. For consistency, all trials were run at the expected resonant frequency of 80 Hz (predicted at $\delta_2=0$). The power actuator drive amplitude was held constant at $\pm 300\mu\text{m}$.

The kinematic model assumes that the central link connecting the two sides of the transmission is rigid and can only move vertically; this means that control actuator motion should have no effect on the opposite wing. To test the validity of this assumption, the trajectories of both wings are tracked at the extremes of the control actuator motion, $\delta_2 = \pm 100\mu\text{m}$ while holding the power actuator signal constant at 80Hz, $\pm 300\mu\text{m}$ (Fig. 13). Analyzing the trajectories of

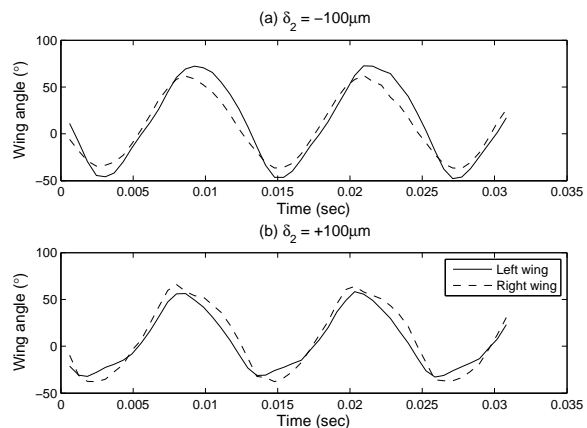


Fig. 13. The trajectories of the left and right wings (attached to the control actuator and ground respectively) are tracked at both extremes of the control actuator motion. This shows that the impact of the control actuator on the opposite wing, while not zero as predicted by the pseudo-rigid body model, is negligible compared to the influence on the proximal wing.

the left (attached to control actuator) and right (attached to ground) wings shows that the lateral stiffness of the transmission is not infinite, as assumed in the kinematics, and the control actuator has a small effect on the opposite wing. However, this change is negligible compared to the effect on the proximal wing – showing changes in amplitude of roughly 30° and 4° on the left and right wings, respectively (Table II).

TABLE II
STROKE AMPLITUDE $\theta_{w,total}$ FOR EACH WING AT EXTREMES OF CONTROL ACTUATOR MOTION

	$\delta_2 = +100\mu\text{m}$	$\delta_2 = -100\mu\text{m}$	$\Delta\theta_{w,total}$
Left wing	89°	118°	29°
Right wing	102°	98°	4°

Once the influence of the control actuator on the two wings has been verified at the motion extremes, tests are then performed over the full range of motion. Again, the power actuator signal is held constant at 80Hz and $\delta_1 = \pm 300\mu\text{m}$ while the control actuator position is varied from $-100\mu\text{m}$ to $+100\mu\text{m}$. The total and average stroke angles of the orthogonally actuated wing are extracted for each trial since they will influence body torque generation; these results are compared to both kinematic and dynamic predictions (Fig. 14). For total stroke angle, the kinematic, dynamic and experimental measurements all show the same trend – control actuator motion increases or decreases stroke angle with $\delta_2 < 0$ or $\delta_2 > 0$ respectively. However, while both kinematic and dynamic models predict a change in the average stroke angle, experimental results show the average angle to hold relatively constant over the range of control actuator motion. This relatively constant nonzero average stroke angle is most likely due to a manufacturing imperfection - a small misalignment when manually mounting the transmission to the airframe and connecting it to the actuators can have a

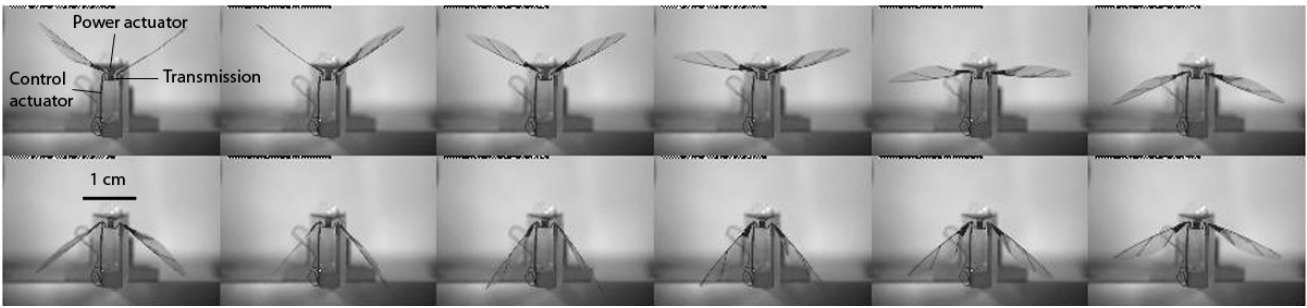


Fig. 12. Frames from a typical high-speed video trial showing the actuated flapping of the wing and passive rotation about the spanwise axis. Flapping is at 110 Hz, video shot at 1600 fps.

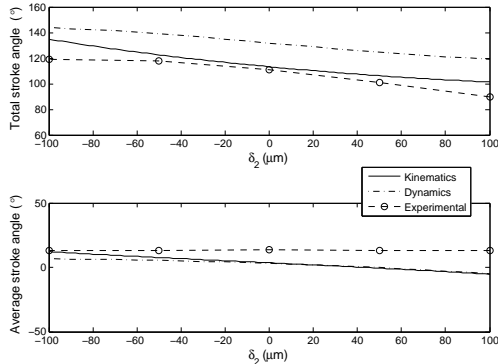


Fig. 14. Measured mean and total stroke angles compared to kinematic and dynamic predictions at 80Hz.

TABLE III

KINEMATIC, DYNAMIC AND EXPERIMENTAL RESULTS FOR EFFECT OF CONTROL ACTUATOR MOTION ON TOTAL STROKE ANGLE AT 80 HZ

Method	$\delta_2 = +100\mu\text{m}$	$\delta_2 = -100\mu\text{m}$	$\Delta\theta_w$
Kinematics	101°	134°	33°
Dynamics	119°	144°	25°
Experimental	90°	119°	29°

non-negligible impact on the neutral stroke angle. Work is ongoing to increase the accuracy and level of automation of assembly steps in order to minimize such errors.

The changes in total stroke angle are summarized in Table III. The observed magnitude of stroke angle is lower than that predicted by both kinematics and dynamics. This can likely be attributed to an over-estimation of the power actuator force and displacement, as well as minor manufacturing defects such as debris and epoxy in the flexure gaps, which can impede motion. However, the observed *change* in total stroke angle over the range of control actuator motion lies about halfway between the kinematic and dynamic predictions.

It is therefore instrumental to eliminate resonant effects by running the tests quasi-statically at a very low frequency (1Hz), at which aerodynamic and inertial forces will be negligible due to the low wing velocity. The same information is then collected over the range of control actuator motion

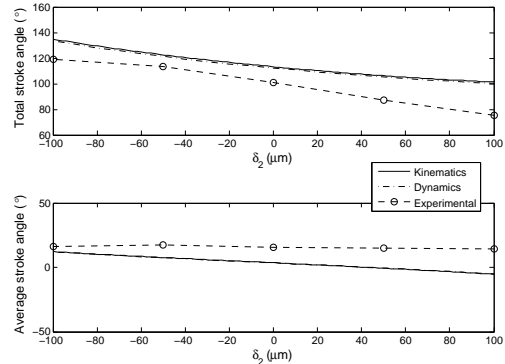


Fig. 15. Measured mean and total stroke angles compared to kinematic and dynamic predictions at 1Hz.

TABLE IV

KINEMATIC, DYNAMIC AND EXPERIMENTAL RESULTS FOR EFFECT OF CONTROL ACTUATOR MOTION ON TOTAL STROKE ANGLE AT 1 HZ

Method	@ $\delta_2 = +100\mu\text{m}$	@ $\delta_2 = -100\mu\text{m}$	$\Delta\theta_w$
Kinematics	101°	134°	33°
Dynamics	101°	134°	33°
Experimental	75°	119°	44°

(Fig. 15). The changes in total stroke angle are summarized in Table IV. As expected, the dynamic model converges to the kinematic model as the drive frequency approaches zero. While both models still overestimate the observed total stroke angle, the effect of the control actuator still follows the same trend. These results justify the use of control actuators to asymmetrically modify wing stroke amplitude. The next step will be to build and test a flightweight version complete with two control actuators, which can be mounted on torque and force sensors to measure changes in lift and body moments.

V. CONCLUSIONS AND FUTURE WORK

The device discussed here functions as a proof-of-concept for biologically-inspired modulation of wing kinematics for a microrobotic fly. This is accomplished by providing primary mechanical power through a large “flight muscle” actuator and fine-tuning kinematics through the use of smaller “con-

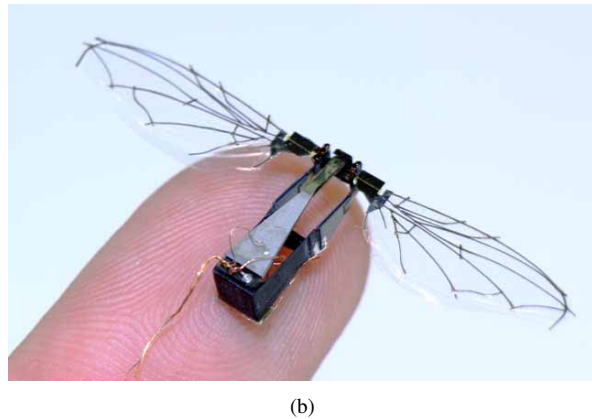
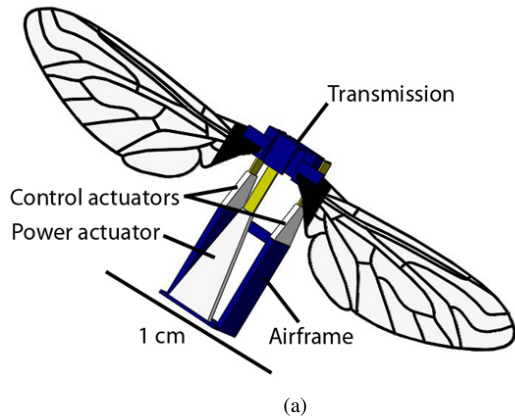


Fig. 16. A concept drawing of the microrobotic fly complete with two control actuators and a new wing design with bio-inspired veination patterns (a), and a first-generation 130mg, 4-cm wingspan prototype fly that will be used to measure body torques generated by control actuator motion (b).

control” actuators. This expanded control gives the designer the ability to directly modulate the kinematics of each wing independently, while still relying on passive dynamics for wing rotation about the spanwise axis, resulting in the indirect ability to control body torques. The device presented here is a simple testbed, not optimized for maximal power density and only having control over one wing. The next steps in the project include optimizing the design of both the power and control actuators and designing a new, lightweight carbon fiber airframe capable of supporting all three actuators (Fig. 16). The fly will be mounted on a torque sensor to measure the body moments that can be generated; this information will be used to create control laws for stabilization about the three rotational axes. The guide wires restricting the original microrobotic fly to vertical translation will gradually be removed, allowing the fly to rotate freely, as the next step toward the development of untethered autonomous MAVs.

VI. ACKNOWLEDGEMENTS

This work was supported in part by the Office of Naval Research (under award number N00014-08-1-0919), Army Research Laboratory (under award number W911NF-08-2-0004), and the National Science Foundation (under award

number CMMI-07466 38). Any opinions, findings and conclusions or recommendations expressed in this material are those of the authors and do not necessarily reflect those of the National Science Foundation.

REFERENCES

- [1] R. Wood, “Liftoff of a 60mg flapping-wing MAV,” in *IEEE/RSJ International Conference on Intelligent Robots and Systems*, 2007, pp. 1889–1894.
- [2] —, “Design, fabrication, and analysis, of a 3DOF, 3cm flapping-wing mav,” in *IEEE/RSJ International Conference on Intelligent Robots and Systems*, 2007, pp. 1576–1581.
- [3] —, “The first takeoff of a biologically inspired at-scale robotic insect,” in *IEEE Transactions on Robotics*, vol. 24, no. 2, 2008, pp. 341–347.
- [4] R. Wood, S. Avadhanula, R. Sahai, E. Steltz, and R. Fearing, “Micro-robot Design Using Fiber Reinforced Composites,” *Journal of Mechanical Design*, vol. 130, pp. 52 304–52 315, 2008.
- [5] D. Campolo, R. Sahai, and R. Fearing, “Development of piezoelectric bending actuators with embedded piezoelectric sensors for micromechanical flapping mechanisms,” in *IEEE International Conference on Robotics and Automation*, vol. 3, 2003, pp. 3339–3346.
- [6] R. Wood, E. Steltz, and R. Fearing, “Optimal energy density piezoelectric bending actuators,” *Sensors and Actuators A: Physical*, vol. A 119, pp. 476–488, 2005.
- [7] H. Tanaka, K. Hoshino, K. Matsumoto, and I. Shimoyama, “Flight dynamics of a butterfly-type ornithopter,” *IEEE/RSJ International Conference on Intelligent Robots and Systems*, pp. 2706–2711, 2005.
- [8] R. Madangopal, G. Student, Z. Khan, and S. Agrawal, “Biologically Inspired Design Of Small Flapping Wing Air Vehicles Using Four-Bar Mechanisms And Quasi-steady Aerodynamics,” *Journal of Mechanical Design*, vol. 127, p. 809, 2005.
- [9] T. Pornsin-Sirirak, Y. Tai, C. Ho, and M. Keennon, “Microbat: A Palm-Sized Electrically Powered Ornithopter,” *Proceedings of NASA/JPL Workshop on Biomimetic Robotics*, pp. 14–17, 2001.
- [10] R. Fearing, K. Chiang, M. Dickinson, D. Pick, M. Sitti, and J. Yan, “Wing transmission for a micromechanical flying insect,” in *IEEE International Conference on Robotics and Automation*, vol. 2, 2000, pp. 1509–1516.
- [11] M. Sitti, “PZT actuated four-bar mechanism with two flexible links for micromechanical flying insect thorax,” in *IEEE International Conference on Robotics and Automation*, vol. 4, 2001, pp. 3893–3900.
- [12] S. Avadhanula, R. Wood, D. Campolo, and R. Fearing, “Dynamically tuned design of the MFI thorax,” in *IEEE International Conference on Robotics and Automation*, vol. 1, 2002, pp. 52–59.
- [13] A. Bergou, S. Xu, and Z. Wang, “Passive wing pitch reversal in insect flight,” *J. Fluid Mech.*, vol. 591, pp. 321–337, 2007.
- [14] M. Dickinson, F. Lehmann, and S. Sane, “Wing rotation and the aerodynamic basis of insect flight,” *Science*, vol. 284, no. 5422, pp. 1954–1960, 1999.
- [15] L. Schenato, X. Deng, and S. Sastry, “Flight control system for a micromechanical flying insect: Architecture and implementation,” in *IEEE International Conference on Robotics and Automation*, vol. 2, 2001, pp. 1641–1646.
- [16] X. Deng, L. Schenato, and S. Sastry, “Hovering flight control of a micromechanical flying insect,” in *Decision and Control*, vol. 1, 2001, pp. 235–240.
- [17] X. Deng, L. Schenato, W. Wu, and S. Sastry, “Flapping flight for biomimetic robotic insects: Part I-system modeling,” *IEEE Transactions on Robotics*, vol. 22, no. 4, pp. 776–788, 2006.
- [18] X. Deng, L. Schenato, and S. Sastry, “Flapping flight for biomimetic robotic insects: Part II-flight control design,” *IEEE Transactions on Robotics*, vol. 22, no. 4, pp. 789–803, 2006.
- [19] M. Dickinson and M. Tu, “The function of dipteran flight muscle,” *Comp. Biochem. Physiol.*, vol. 116A, no. 3, pp. 223–238, 1997.
- [20] S. Avadhanula, “Design, fabrication and control of the micromechanical flying insect,” Ph.D. dissertation, University of California, Berkeley, 2006.
- [21] C. Ellington, “The aerodynamics of hovering insect flight. IV. aerodynamic mechanisms,” *Philosophical Transactions of the Royal Society of London. Series B, Biological Sciences*, vol. 305, no. 1122, pp. 79–113, 1984.